

Vibronic quantum dynamics of ultralong-range high- ℓ Rydberg molecules

Felix Giering,¹ Rohan Srikumar^{ORCID},¹ and Peter Schmelcher^{ORCID}¹

¹*Zentrum für Optische Quantentechnologien, Universität Hamburg,
Luruper Chaussee 149, 22761 Hamburg, Germany*

(Dated: March 17, 2026)

We investigate the non-adiabatic quantum dynamics of ultralong-range Rydberg molecules using a vibronically coupled two-channel treatment. The two channels are composed of coupled trilobite and butterfly electronic states, formed as a result of S -wave and P -wave scattering of high angular momentum Rydberg electrons with perturbing ground state atoms. Within the Born-Oppenheimer treatment, the P -wave scattering channel introduces an adiabatic decay pathway that affects the stability and lifetimes of trilobite states. Our numerical results show that the vibronic coupling is dependent on the principal quantum number n , and for certain n there is non-adiabatic stabilization against internal molecular decay, facilitating previously studied dynamical effects in pure trilobite molecules. Apart from the internal diffraction effect we also observe interesting multi-well tunneling effects, during low-energy oscillations for certain n -values. Our work serves to highlight that the unique R -dependent electronic structure of these polar molecules, along with high level densities, promise many exciting dynamical effects.

I. INTRODUCTION

The ability to engineer Rydberg excitations in ultracold atomic gases has sprouted a completely new branch of molecular physics, where long-range bound states are formed due to unconventional binding mechanisms [1–7]. For example, trilobite and butterfly molecules are formed when a Rydberg atom with high electronic angular momentum (ℓ) undergoes S -wave and P -wave scattering from a nearby ground state atom (perturber), respectively [1, 2]. They feature exceptionally high dipole moments [8, 9] and micrometer scale bond-lengths and have been found useful in precision spectroscopy [10, 11], prospective preparation of ultracold neutral plasmas [12], and measuring three-body correlations [13, 14]. Moreover, these ultralong-range Rydberg molecules (ULRMs) [15–17] offer a great testbed to study unique and exaggerated quantum dynamics [18–20]. Recent numerical simulations show that nuclear wavepackets propagating through the undulating trilobite potential undergo back scattering, thereby creating an internal diffraction effect wherein the electronic structure of the dimer diffracts its own radial motion [20], a phenomena unobserved in standard molecular physics.

The traditional approach to study the quantum dynamics of ULRM is through the use of the Born-Oppenheimer (BO-) approximation [21]. However, recent studies show that non-adiabatic effects are ubiquitous in such systems, mainly due to avoided crossings introduced by high- ℓ states, as well as the high density of electronic states that are not energetically well-separated [22, 23]. Such avoided crossings can be highly singular, sometimes forming conical intersections, when the principal quantum number n of the Rydberg atom is taken as a synthetic dimension [24, 25]. In alkali ULRMs, the P -wave butterfly potential induces an avoided crossing to the trilobite potential, introducing an adiabatic decay pathway. Experimental observations of highly excited non-adiabatic resonances for selected n -values stabilized

against internal adiabatic decay [26], confirm the necessity to go beyond single channel BO-approximation to accurately model these molecules.

The multichannel wavepacket dynamics in ULRM remains largely unexplored. Previous works have mainly utilized Landau-Zener based semiclassical analysis [24, 27, 28], or limited themselves to spectral calculations [22, 23, 26]. An exact quantum dynamical study will be able to validate previous semiclassical approximations, as well as point out why and where they fail. Moreover, it confirms whether or not previously simulated single channel dynamical effects like internal diffraction [20], is suppressed due to non-adiabatic effects. In conventional molecules vibronic dynamics facilitate many well documented phenomena like ultrafast non-radiative transitions [29–31], surface hoppings [32, 33], and predissociation [34, 35], which are not explainable by adiabatic physics. But highly polar ULRMs, with large bond lengths, and high level densities could exhibit new vibronic dynamical effects that are not seen in regular molecules.

In this work we study the dynamics of ⁸⁷Rb dimers, in coupled trilobite and butterfly configurations using a two channel treatment that considers the mixing of nuclear and electronic motion. A comprehensive theoretical study of this system, which looks at the structure of electronic states and non-adiabatic couplings as a function of n , develops diabaticization strategies to work around singular couplings, and calculates the molecular vibronic spectra has already been presented [22]. Here we perform wave-packet dynamics, with vibrational Gaussian states initialized in the trilobite PEC, radially far off from any avoided crossings. As the wavepackets probe the avoided crossing, we see the onset of n -dependent non-adiabatic transitions between different PECs. We use the probability distribution function in position and momentum representations, as well as the evolution of different electronic state populations, to characterize vibronic effects for each n . For some n , the propagating diffraction effect

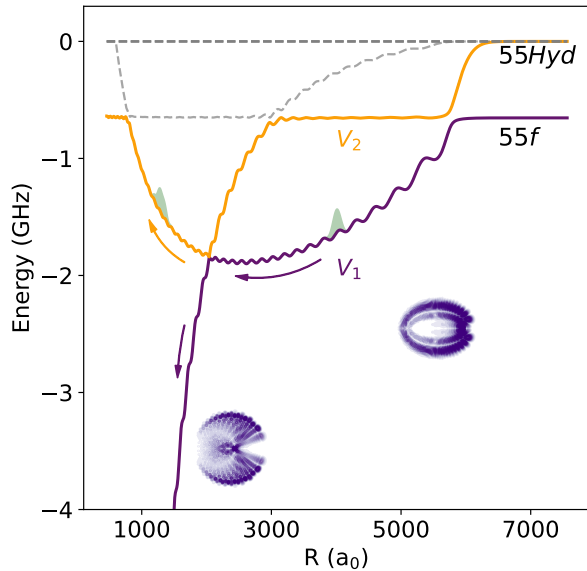


FIG. 1. The Born-Oppenheimer potentials of the $n=55$ ULRM, obtained by solving the electronic Schrödinger equation. The two-state system corresponds to the highlighted V_1 (violet) and V_2 (orange) potentials, ignoring the grey curves for low energy dynamics. The wavepackets and arrows are used to illustrate the possible trajectories of a time evolving nuclear wavefunction. The probability density plots of $\phi_1(\mathbf{r}, R)$ (corresponding to the PEC V_1) calculated at $R=1400$ a_0 and $R=4880$ a_0 , portray the change of electronic structure from trilobite to butterfly states as R changes.

is conserved against internal molecular decay due to non-adiabatic stabilization. We also present here, a unique multiwell tunnelling phenomenon due to low energy oscillations around the minima of the trilobite potential. The calculations presented here neglect the fine and hyperfine structure of the constituent atoms for the sake of ease. Inclusion of the spin couplings would necessitate more complex multichannel treatment, that is of great interest for a future study.

This work is organised as follows. Section II presents the theoretical and computational framework, introducing the general molecular Hamiltonian and nonadiabatic couplings in subsection II A, discussing the specific electronic interactions in the ULRM in subsection II B, and describing the two-channel vibronic dynamics in subsection II C. Section III presents the results of our numerical simulation, starting from the potential energy structure in subsection III A, the two channel wavepacket dynamics in subsection III B, and multiwell tunnelling effects in subsection III C. The conclusions and outlook of our work are given in section IV.

II. THEORETICAL AND COMPUTATIONAL FRAMEWORK

We begin by formulating the molecular Hamiltonian and the corresponding time dependent Schrödinger equation which allows us to study the internal molecular dynamics of ULRM. We then discuss the Born-Oppenheimer approximation, the emergence of nonadiabatic couplings between BO adiabatic electronic states, and the associated diabatisation procedure which is crucial for constructing a smooth multi-channel representation. Subsequently, we highlight the electronic structure of the ULRM and the calculation of adiabatic states and PECs. Finally, we establish the two-channel vibronic system and describe the numerical propagation scheme, where complex absorbing potentials are employed to avoid artificial reflections at the grid boundaries.

A. Molecular Hamiltonian and nonadiabatic couplings

We start by considering two ^{87}Rb atoms, one of which is excited to the Rydberg electronic state. Let us define R as the internuclear separation between the ionic core and the neutral atom (taken along the z -axis, with the Rydberg core at the origin), and \mathbf{r} as the coordinate of the Rydberg electron with respect to the Rydberg core. The internal molecular dynamics (in atomic units) in the body-fixed frame is then governed by the time-dependent Schrödinger equation

$$i \frac{\partial}{\partial t} \psi_m(\mathbf{r}; R \mathbf{e}_z, t) = \hat{H} \psi_m(\mathbf{r}; R \mathbf{e}_z, t), \quad (1)$$

with ψ_m being the molecular wavefunction and \hat{H} the molecular Hamiltonian given by:

$$\hat{H} = -\frac{\nabla_R^2}{2\mu} - \frac{\nabla_r^2}{2} + V_{\text{Ryd}}(\mathbf{r}) + V_{\text{ea}}(\mathbf{r}; R \mathbf{e}_z) \quad (2)$$

where μ is the reduced mass of the system. The first two terms of the Hamiltonian describe the kinetic energy operators corresponding to the nuclei and the Rydberg electron respectively. Moreover, $V_{\text{Ryd}}(r)$ represents the interaction between the Rydberg electron and the ionic core and $V_{\text{ea}}(\mathbf{r}; R)$ accounts for the interaction between the Rydberg electron and the perturbing ground state atom. The last three terms of Eq. 2 separately form the electronic Hamiltonian $H_{\text{el}}(\mathbf{r}; R)$. Solving the electronic Schrödinger equation parametrized by R yields

$$H_{\text{el}}(\mathbf{r}; R) \phi_n(\mathbf{r}; R) = V_n(R) \phi_n(\mathbf{r}; R), \quad (3)$$

where $V_n(R)$ are the adiabatic potential energy curves and $\phi_n(\mathbf{r}; R)$ are the corresponding electronic states. Since $\{\phi_n\}$ forms a complete orthonormal basis (popularly known as the Born-Oppenheimer basis), any given molecular wavefunction can be expanded as

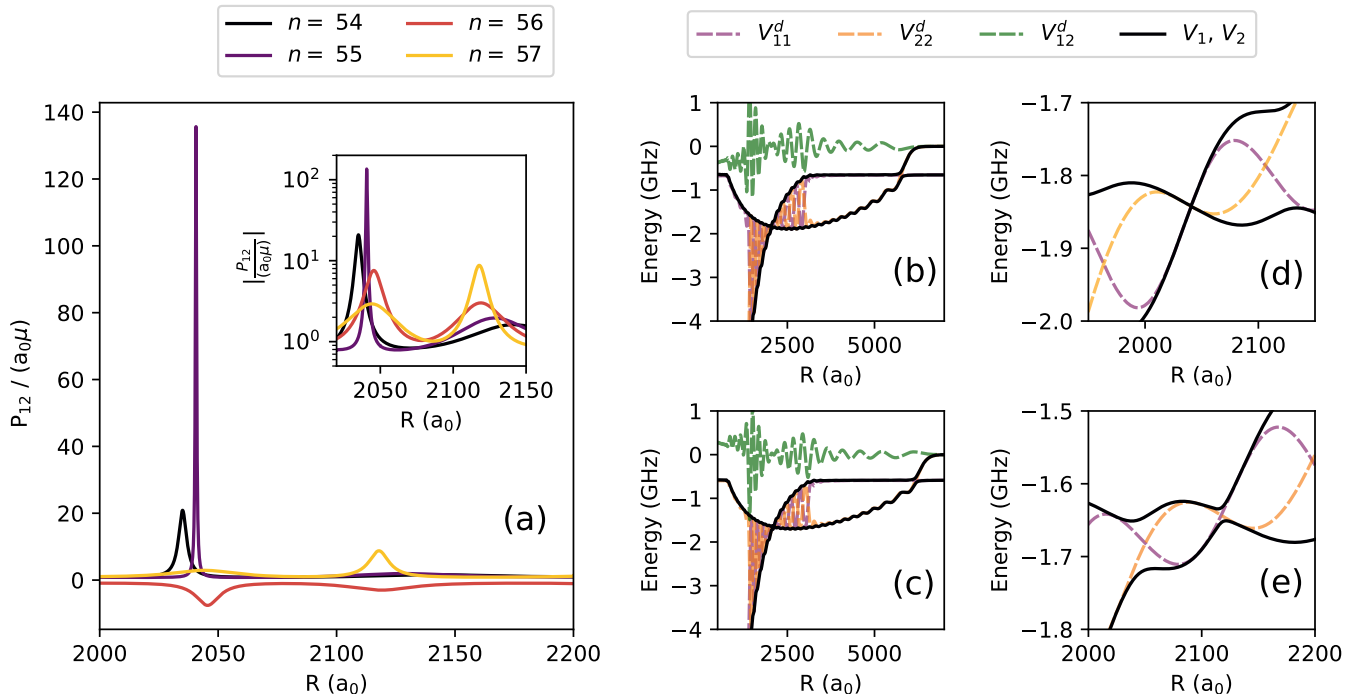


FIG. 2. (a) The first order derivative coupling element $P_{12}/\mu a_0$ as a function of the internuclear distance R , for varying n -values. The inset depicts the magnitude of P_{12} with log-scaling of the y -axis. The adiabatic and diabatic PECs of the $n = 55$ and $n = 57$ ULRM are shown in (b) and (c) respectively, with (d) and (e) being the corresponding magnified plots showcasing the avoided crossing.

$\Psi_m = \sum_n \chi_n(R) \psi_n(\mathbf{r}, R)$ [36]. Here $\chi_n(R)$ are the R -dependent expansion coefficients that represent the nuclear wavefunction.

Inserting this Born-Oppenheimer expansion in Eq. 2, integrating out the electronic states and rearranging the terms, we get the multichannel Schrödinger equation

$$-\frac{1}{2\mu}(\nabla_R + \hat{P})^2 \chi + \hat{V} \chi = i \frac{\partial}{\partial t} \chi \quad (4)$$

where χ is a vector of all χ_n , \hat{V} is a diagonal operator containing all V_n and \hat{P} is the first order non-adiabatic coupling operator whose matrix elements are given by

$$P_{\mu\nu}(R) = \int \phi_\mu(\mathbf{r}; R) \partial_R \phi_\nu(\mathbf{r}; R) d\mathbf{r}. \quad (5)$$

The P -matrix elements appear as off-diagonal terms in the nuclear kinetic energy operator, effectively coupling different adiabatic electronic channels. Note that a more elaborate discussion on derivative couplings can be found in our previous works [22, 23], and methodical derivations that show how to obtain Eq. 4 from Eq. 2 are discussed in standard textbooks [37, 38]. In the Born-Oppenheimer approximation, the non-adiabatic term \hat{P} is completely ignored, resulting in decoupled single channel equations that describe the nuclear dynamics of the

molecule. This framework provides a natural first description of ultralong-range Rydberg molecules, where the diatomic system time-evolves in a given potential energy curve defined by its time-independent electronic state.

However, non-adiabatic couplings become particularly pronounced near avoided crossings of the adiabatic PECs. Our previous works highlight such cases where a non-adiabatic treatment of the ULRM was necessary due to the presence of avoided crossings [22, 23, 39]. In such regions the BO approximation breaks down due to singular or rapidly varying couplings, and the adiabatic basis becomes ill-suited for describing nuclear dynamics. To remedy this, it is advantageous to perform a basis transformation such that the nuclear kinetic couplings are replaced with off-diagonal potential terms. Given that Eq. 4 is invariant under unitary transformations, any \hat{U}_d which satisfies the condition $\nabla \hat{U}_d = -\hat{P} \hat{U}_d$ will force the derivative couplings to become zero, and is popularly known as a diabatic transform [37, 40]. This allows us to rewrite Eq. 4 as

$$-\frac{1}{2\mu} \nabla_R^2 \chi^d + \hat{V}^d \chi^d = i \frac{\partial}{\partial t} \chi^d, \quad (6)$$

where $\chi^d = \hat{U}_d \chi$ are called the diabatic states and the constituents of $\hat{V}^d = \hat{U}_d^\dagger \hat{V} \hat{U}_d$ are called diabatic PECs.

In the general case of polyatomic molecules, \hat{U}^d is not uniquely defined and approximate path-dependent diabatization schemes are used to perform vibronic dynamics. Fortunately, if the system is one-dimensional (like a diatomic molecule) one can always find a unique diabatization scheme numerically, although this becomes computationally tedious with increasing number of highly coupled channels. Furthermore, in the simplest description of a vibronic system, i.e. a two channel system with a single parameter R , the diabatic transform is a basic unitary rotation where the rotation angle is given by

$$\theta(R) = \int_R^\infty P_{12}(R_1) dR_1. \quad (7)$$

With the two-channel diabatic framework established, the next step is to specify the electronic interactions responsible for binding in ultralong-range Rydberg molecules.

B. Electronic interaction

The electronic Hamiltonian for the ULRM is given by $H_{el} = H_{Ryd} + V_{ea}$, where H_{Ryd} describes the Rydberg atom and V_{ea} describes the low energy electron-perturber scattering interaction. The s-wave and p-wave scattering can be modeled using Fermi-type pseudo-potentials [41, 42] such that

$$V_{ea}(\mathbf{r}; R) = 2\pi a_s(k)\delta(\mathbf{r} - R\mathbf{e}_z) \quad (8)$$

$$+ 6\pi a_p(k)\nabla_r\delta(\mathbf{r} - R\mathbf{e}_z)\nabla_r, \quad (9)$$

with a_s and a_p denoting the energy dependent s-wave scattering length and p-wave scattering volume respectively (scattering length taken from [11]). The electron wavenumber k can be semi-classically approximated by $k = (2/R - 1/n^2)^{1/2}$, where n is the principal quantum number of the Rydberg excitation. In the spin triplet configuration, both a_s and a_p have negative values, facilitating an attractive interaction and binding the molecule. The unperturbed Rydberg electron states $\{\phi_{nlm}\}$ are described by the principal and angular momentum quantum numbers (n, l, m) respectively. Since the internuclear axis is taken to be along the z-axis, only atomic states with $m=0$ contribute. They form the eigenbasis of the electronic Rydberg Hamiltonian with the corresponding energies $E_{nl} = -(n - \delta_l)^{-2}/2$, with μ_l denoting the l -dependent quantum defect [43]. In rubidium the low angular momentum states ($l \leq 3$) exhibit finite quantum defects, energetically shifting them away from the near-degenerate hydrogenic manifold of high- l states. These low- l states form shallow PECs allowing a few bound states. The high- l states however is hybridized by the perturber, resulting in deep potentials that can hold hundreds of bound states. The most prominent of these high- l states are the so-called

trilobite and butterfly molecules, split from the hydrogenic manifold due to S -wave and P -wave electron-atom scattering. Recent works have already characterized the vibronic structure of the coupled trilobite-butterfly system, successfully showing the impact of these avoided crossings in the calculated and observed spectra [22, 26]. In this work, we extend these studies by performing nuclear dynamics simulation of the molecule in the coupled butterfly-trilobite configuration.

Here we mention that the state of the art Green's function methods [44] provide a more accurate description of the electronic structure of the ULRM, however they do not allow for the calculation of the electronic states and their couplings so far. Moreover, spin-orbit and hyperfine interactions [45, 46] are neglected in our model so that a two channel treatment becomes possible. Fortunately, recent works show that a simple spin-less two-channel system can already explain observed non-adiabatic phenomena in ULRM very well [26]. Hence, we choose to focus only on the two-channel case relevant for the trilobite-butterfly interaction, which is well-justified when the dynamics is dominated by a pair of energetically isolated states with localized coupling, while all other channels remain weakly interacting and well-separated.

C. Computational approach: two-channel vibronic dynamics

We start by obtaining the adiabatic PECs and the corresponding electronic wave functions for a given n by diagonalizing the electronic Hamiltonian within a finite Rydberg basis $\{\phi_{n'l'0}\}$ that includes all states with $n' \in \{n-2, n+2\}$. Then we proceed to calculate the diabatic transform and the diabatic PECs for the two-channel trilobite-butterfly system. The initial nuclear wavepacket is a Gaussian function in the first adiabatic channel, i.e. $\chi^a = (\chi_1^a, \chi_2^a)^T$ with

$$\chi_1^a(R, 0) = \frac{1}{(\pi\sigma^2)^{1/4}} \exp\left[-\frac{(R - R_0)^2}{2\sigma^2}\right], \quad (10)$$

$$\chi_2^a(R, 0) = 0. \quad (11)$$

Initializing the wavepacket in the adiabatic basis allows us to populate the trilobite or butterfly state selectively, which is made difficult in the diabatic basis due to strong mixing of electronic states. The adiabatic wavefunction is then transformed into the diabatic basis via $\chi^d(R, t = 0) = \hat{U}(R)\chi^a(R, t = 0)$. We then propagate $\chi^d(R, t)$ using the diabatic Schrödinger equation given by Eq. 6.

Time propagation of the wavepacket is performed using the Crank-Nicolson scheme [47, 48], which provides stable and unitary time evolution. The second deriva-

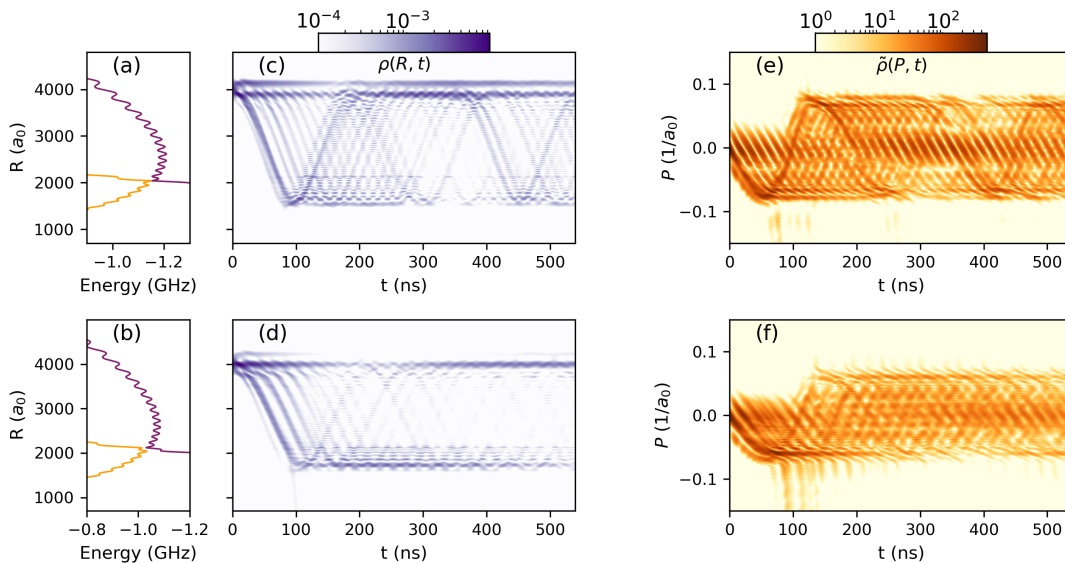


FIG. 3. Two channel wavepacket diffraction dynamics. The potential energy structure of the $n = 55$ and $n = 57$ ULRM in the relevant region, are shown in (a) and (b). The time evolving total probability density $\rho(R, t)$ in the position representation is shown for $n = 55$ (c) and $n = 57$ (d). The corresponding total probability density in momentum representation, i.e. $\tilde{\rho}(P, t)$ is shown for $n = 55$ (e) and $n = 57$ (f).

tive is evaluated using finite differences of tenth order [49], ensuring high numerical accuracy even for small grid spacings. In our simulations, we use a grid spacing of $\Delta R \approx 1a_0$ and a time step of $\Delta t \approx 0.001$ nanoseconds, chosen such that the energy scale of the system is well resolved [50]. Quantum reflection at the grid boundaries can lead to unphysical interference in the wavepacket dynamics. To prevent this, we employ a complex absorbing potential (CAP) [51, 52] that smoothly absorbs the wavefunction near the grid edge and thus simulates the molecular decay due to the open channel nature of our system. See Appendix A for more details on the CAP implementation.

At every time step the total probability density is calculated to be

$$\rho(R, t) = |\chi_1^d(R, t)|^2 + |\chi_2^d(R, t)|^2, \quad (12)$$

and the diabatic channel populations are calculated to be

$$p_i^d(t) = \int dR |\chi_i^d(R, t)|^2. \quad (13)$$

One can perform an inverse diabaticization transform $\chi^a = U^\dagger \chi^d$ to obtain the adiabatic channel populations

$$p_i^a(t) = \int dR |\chi_i^a(R, t)|^2 \quad (14)$$

which help us understand how the electronic states are mixed as a function of time due to vibronic dynamics. Due to the CAP the time evolution is no longer unitary

and the total population

$$p_{tot}(t) = \sum_i p_i^a(t) = \sum_i p_i^d(t) \quad (15)$$

does not maintain unit value, as the wavefunction is absorbed at the end of the grid. Note that the total probability density $\rho(R)$ as well as the total population p_{tot} are basis independent quantities and hence invariant under the diabaticization transform. To understand the scattering effects in the two-channel problem, one can use the Fourier transform to calculate the momentum space wavefunction $\tilde{\chi}(P, t) = \mathcal{F}[\chi(R, t)]$ in each channel, and consequently obtain the total momentum space probability distribution $\tilde{\rho}(P, t) = |\tilde{\chi}_1(P, t)|^2 + |\tilde{\chi}_2(P, t)|^2$, where P is the momentum of the nuclear wavepacket. In the next section, we numerically investigate the vibronic dynamics of the ULRM within the context of internal diffraction dynamics, multi-well tunnelling effects, and non-adiabatic decay.

III. RESULTS AND DISCUSSIONS

In the following section, we discuss the results of our numerical simulations. We start with the adiabatic and diabatic potential energy curves as well as the non-adiabatic couplings in the coupled trilobite-butterfly system. We then study the multichannel internal diffraction effect, and analyze the n -dependent non-adiabatic corrections by studying the probability density functions of the evolving wavepacket as well as the population dynamics. Finally, we unravel multiwell tunneling effects in the low

energy oscillations around the minima of the trilobite potential.

A. Potential energy structure

We start with a brief review of the electronic structure of high- ℓ ULRM. Figure 1 shows the adiabatic PECs for an $n = 55$ ULRM obtained by diagonalizing the electronic Hamiltonian, with the exemplary n -value being ideal for observing internal diffraction effects. The adiabatic PECs relevant to the two-state model are highlighted in color (V_1 as blue and V_2 as red), whereas states corresponding to the grey adiabatic curves are not considered in further calculations. When the perturber is radially outside the Rydberg atomic orbital, ($R \geq 2n^2$), the adiabatic potentials V_1 and V_2 energetically coincide with the unperturbed $55f$ quantum defect state and the high- ℓ hydrogenic state, respectively. At smaller R -values the S -wave scattering hybridizes the hydrogenic manifold, introducing an avoided crossing between the trilobite PEC and the $\ell = 3$ PEC, forming the V_1 potential. Here, we choose to focus only on the two highlighted curves as a first approximation. Without the P -wave interaction, V_1 would be a pure trilobite curve with the structure of an anharmonic envelop overlaid with an oscillatory potential [20]. However, the P -wave shape resonance induces a steeply descending butterfly potential that forms a narrow avoided crossing between V_1 and V_2 . After the avoided crossing V_1 adiabatically acquires the P -wave character, eventually causing internal molecular decay due to autoionization or ℓ -changing collisions [27]. However, we know that a narrow avoided crossing enhances the vibronic coupling terms, enabling the non-adiabatic transition from V_1 to V_2 , possibly offering a stabilizing mechanism against internal molecular decay. The adiabatic electronic probability density plots of $\phi_1(\mathbf{r}, R)$ calculated sufficiently before and after the avoided crossing, show how ϕ_1 adiabatically changes from trilobite to butterfly configuration.

Figure 2(a) shows the non-adiabatic coupling P_{12} between the selected states ϕ_1 , ϕ_2 for the selected range of n . We scale P_{12} by $1/\mu a_0$ to analyze the energy contribution of the non-adiabatic coupling term as it appears in the Hamiltonian, in GHz units. We see that the derivative coupling strongly depends on n , displaying an order of magnitude difference between the most non-adiabatic ($n = 55$) and most adiabatic ($n = 57$) cases. This is highlighted in the inset, where the y -axis is log-scaled to simultaneously show the smaller structures in energy. From a semi-classical perspective, the absolute value of the P_{12} , at the avoided cross massively impacts the probability that nuclei perform a non-adiabatic jump, i.e. Landau-Zener (LZ-) transition from ϕ_1 to ϕ_2 . However, we already see from the inset that the calculated derivative couplings do not form a Lorentzian curve, as

is typical in LZ-transitions. Figures 2(b) and 2(c) show the diabatic PECs (dashed curves) and the adiabatic PECs (solid black curves) for $n = 55$ and $n = 57$ respectively. Primarily, we see that the highly oscillatory (diagonal) diabatic PECs start deviating from their adiabatic counterparts, far away from the avoided crossing ($> 1000a_0$). This is accompanied by the off-diagonal potentials acquiring large non-zero values away from the avoided crossing. Moreover, we see that the global structure of the diabatic curves look reasonably similar between $n = 55$ and $n = 57$, despite a large difference in the magnitude of derivative couplings. However, the magnified plots 2(c) and (d) do show that adiabatic PECs exhibit a narrow near-exact crossing for $n = 55$, and a wider avoided crossing for $n = 57$. This validates the large difference in the magnitude of P_{12} for the two n -values. To summarize, the non-adiabatic couplings, and the diabatic potentials of the two-channel system deviate considerably from traditional molecular physics, or Landau-Zener models. A more detailed analysis of the vibronic couplings between trilobite and butterfly potentials can be found elsewhere (see Ref. [22]). Note that the exact structure of the diabatic potentials varies considerably depending on the number of channels used in diabatization. In reality, the highly polar electronic states are non-adiabatically coupled to other quantum defect states, as well as the quasi-degenerate manifold. To explain higher dynamics spanning the entire potential depth, one would need to incorporate higher quantum defect states and the unperturbed high- ℓ manifold into a multichannel model. Fortunately, the internal diffraction dynamics we probe requires relatively lower kinetic energies [20]. Since we see that the non-adiabatic couplings are still maximal at the avoided crossing, a two-channel model that considers the avoided crossing should give us a reliable semi-quantitative model for the problem at hand.

B. Two channel wavepacket dynamics

We begin our simulation of the wave-packet dynamics, by initializing the nuclear wavefunction as a Gaussian state in the V_1 adiabatic PEC, corresponding to the ϕ_1 electronic state. The initial position and width of the Gaussian are taken to be so that the ensuing dynamics display internal diffraction effects. This is because the oscillatory structure of the trilobite potential acts as a diffraction grating in momentum space. The anharmonic envelope of the pure trilobite PEC allows the wavepacket to gain momentum as it traverses down the potential, consequently scattering off the oscillatory structure of the PEC. At appropriate width and momenta, the consequent coherent back-scattering causes the wavepacket to appear as a propagating diffraction pattern. A comprehensive analysis of this phenomena is presented elsewhere (see Ref. [20]), including the appropriate initial parameters needed to observe this effect. Here we build upon the previous work, and take the required parameters needed

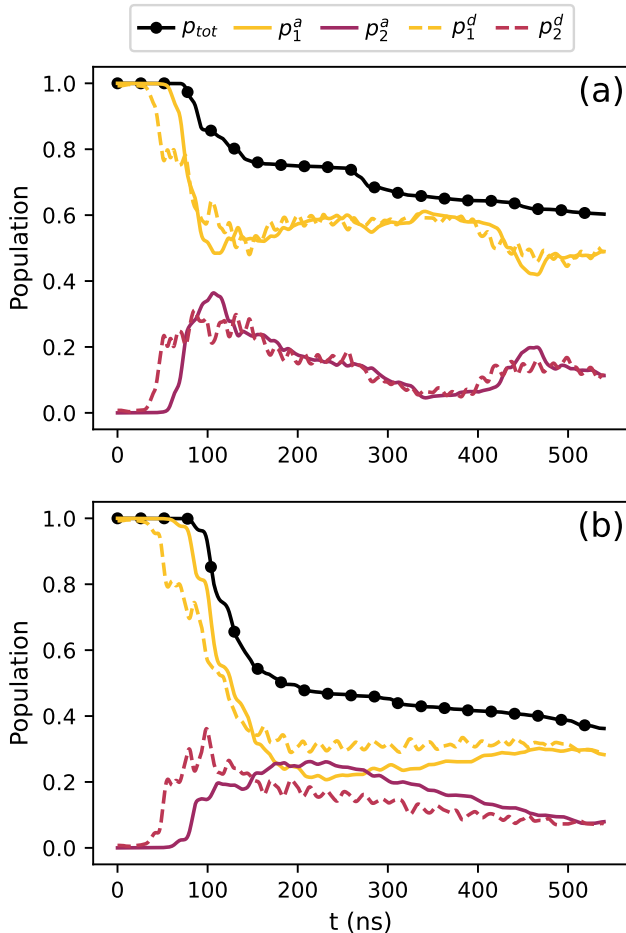


FIG. 4. Time evolution of the diabatic populations p_d (dashed curves), and the adiabatic populations p_a (solid curves) for channel 1 and 2, as well as the the total population p_{tot} (dotted curve). (a) Depicts the population dynamics for $n = 55$, and (b) depicts the population dynamics for $n = 57$.

to observe diffraction, as given. Our aim then, is to see how the vibronic coupling between trilobite and potential affects the previously simulated diffraction dynamics. We try to analyze the n -dependence of the vibronic corrections, by contrasting the $n = 55$ case with $n = 57$, featuring the most and the least non-adiabatic coupling strength at the avoided crossing, respectively.

The relevant potential energy structure of the $n = 55$ and $n = 57$ molecule are shown in figure 3(a) and (b). We choose to initialize the Gaussian wavepacket $\chi_1^a(t = 0)$ (Eq. 11), with $\sigma = 100a_0$, and $R_0 = 4000a_0$. At the given R_0 the diabatic and adiabatic PECs coincide and show a predominant trilobite character. Figure 3 (c) and (d) show the resulting time evolving probability density functions for $n = 55$ and $n = 57$, in position representation. As expected, simulations with both the n -values exhibit a propagating diffraction pattern for $t < 100$ nanoseconds, until they probe the avoided crossing. We see that $n = 55$ continues to exhibit propagating wavepacket dynamics

mimicking the pure trilobite case, although there is a noticeable decrease in the contrast of the pattern compared to the single channel case. This can be explained by the consistent non-adiabatic transition of the nuclear wavepacket between V_1 and V_2 PECs due to the near exact crossing, so that the nuclear wavepacket effectively experience a pure trilobite potential, despite the actual wavepacket dynamics occurring on coupled channels. On the other hand, the $n = 57$ case, with a wider avoided crossing, show a much clearer diminishing of the diffraction pattern after the first crossing. As the wavepacket keeps oscillating it probes the crossing multiple times, thereby destroying the diffraction pattern. When analyzing the dynamics in the momentum space representation (see figure 3 (e) and (f)), we see that the diffraction pattern is more coherent for the the n -value with the more narrow crossing. In addition, when the wavepacket reaches the avoided crossing for the first time, we see that a considerable fraction of the wavepacket gain momentum and escape the propagating diffraction pattern. This is because the nuclei which follow the P -wave decay pathway, experience a steep drop in the potential, resulting in the wavefunction gaining more momentum before it is eventually absorbed by the CAP. This phenomena is more dramatically observed in the case of $n = 57$ due to the wider avoided crossing facilitating more adiabatic decay.

We now focus on the dynamics of the population calculated using aforementioned formulae (Eq. 13 - Eq. 15). Figure 4 (a) and (b) shows the total population (marked \bullet), as well as the channel populations in adiabatic (solid lines) and diabatic (dashed lines) representations. For both n -values, the total population is constant (unit value) for the first 100 nanoseconds, until the wavefunction probes the avoided crossing. The population starts decreasing as expected, when the wavepacket is absorbed by the CAP after the avoided crossing. We also see that the population in the adiabatic channels start mixing slightly before the total population decrease. This corresponds to the short time dynamics that characterize the transfer of population from the trilobite to the butterfly state near the avoided crossing. The diabatic channel populations however, start mixing much before the wavepackets reach the avoided crossing, in accordance with our analysis of extended off-diagonal non-adiabatic couplings in the previous section. This hints at the non Landau-Zener nature of the mathematical model used. Comparing figure 4 (a) to (b), we see that the decrease in total population is indeed more prominent for $n = 57$, due to the wider avoided crossing.

C. Multiwell tunneling dynamics

Finally, we move on from higher energy vibronic dynamics, and shift our focus to low energy dynamics between different adjacent wells of PEC. Figure 5 (a) shows the adiabatic potential energy structure of the $n = 49$

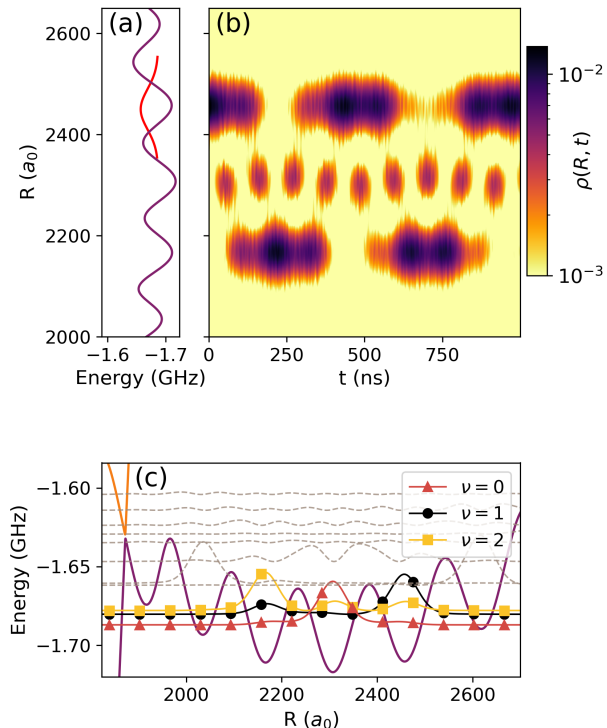


FIG. 5. Multi-well interference effects due to low energy dynamics. (a) Shows the adiabatic potential energy curve V_1 for the $n = 49$ ULRM, along with probability density of the initial Gaussian wavepacket $\rho(R, t = 0)$. (b) The time evolving total probability density $\rho(R, t)$. (c) The vibronic molecular resonances (dashed lines). The three bound eigenstates responsible for the observed multiwell dynamics are highlighted and labelled.

ULRM near the trilobite energetic minima. We probe this region by initializing the nuclear wavepacket as a Gaussian centered around $R = 2450a_0$, with $\sigma = 40a_0$ (red curve in 5 (a)). The ensuing dynamics is shown in figure 5 (b), where we see a periodic interference pattern that spans three different wells. The pattern exhibits two different periods, with most of the population tunneling between next-nearest neighbouring wells. But some of the population periodically localizes in the intermediate well with a pulsing period almost twice as large as the tunneling period. The pattern can be mainly explained using the phase relations between the responsible eigenstates (solid lines in 5 (c) marked as $\nu = 0, 1, 2$), that have a high overlap with the initial Gaussian. The other states only marginally contribute to the dynamics (dashed lines), due to negligible overlap with the initial wavefunction. While the highlighted bound vibronic states are centered around separate adiabatic potential wells, the wavefunction is clearly localized across other neighboring wells. This partial delocalized structure, along with very low level splitting leads to very interesting multi-well tunneling dynamics. The three eigenstates with the largest overlap with the initial wavepacket

have energies $E_0 = -1.687$ GHz, $E_1 = -1.680$ GHz and $E_2 = -1.678$ GHz. The slow tunneling between the two outer wells is mainly governed by the interference between the first and second excited states. Their small splitting of $E_2 - E_1 = 0.002$ GHz corresponds to an interference frequency of about 2 MHz, giving rise to a tunneling timescale of roughly 500 ns. In contrast, the faster pulsation of probability density in the central well arises mainly from the interference between the ground and second excited states. The larger splitting of $E_2 - E_0 = 0.009$ GHz corresponds to a frequency of 9 MHz, which explains the shorter modulation period of about 110 ns visible in figure 5 (b).

Such dynamical features mainly emerge for $45 < n < 50$, where the potential depth of the wells, and the relative heights between wells, facilitate fully bound vibrational states that extend across multiple adjacent potential wells.

IV. CONCLUSION AND OUTLOOK

Our work presents the first step in the study of multichannel vibronic dynamics in ULRM. We started by constructing a two-channel diabatic model from the coupled trilobite-butterfly system, and then proceed to numerically simulate the propagation of nuclear wavepackets using a Crank-Nicolson scheme. The wavefunction was initialized as a Gaussian, with appropriate mean and variance needed to facilitate previously studied diffraction effects. Once the wavepacket escapes into the butterfly channel and reaches small R -values, CAPs were used to simulate an absorbing wall (emulating internal molecular decay). We observed the two-channel analog of the diffraction effect with n -dependent non-adiabatic corrections. For n -values with extremely narrow avoided crossings, the propagating diffraction pattern is non-adiabatically stabilized against decay. For n -values with wide avoided crossings, larger fractions of the nuclear wavepacket is allowed to escape adiabatically. However, the high level density and delocalized non-adiabatic coupling suggest that high energy oscillations might need more than two-channels for accurate simulation. In the case of very low-energy dynamics, accurately simulated using a few single channel vibrational states, we observe interesting multi-well interference patterns.

In principle, the results obtained here should be experimentally observable using state-of-the-art pump-probe schemes, as discussed in our previous work [20]. The preparation of the initial states, as well as certification of the dynamical effects can be performed using bound states in low- ℓ ULRM. Moreover, the two-channel model provided can also be used to simulate pre-dissociation dynamics and ℓ -changing collisions [12, 27] with low- ℓ quantum defect states. From a theoretical perspective, a more ambitious extension of this work is to develop a multichannel model, considering the effect of the quasi-degenerate manifold, as well as couplings to nearby n -

values. This will allow us to simulate vibronic dynamics in high- ℓ and low- ℓ molecules with quantitative rigor. Future theoretical investigations can also consider introducing an external electric field, breaking the spherical symmetry of the systems and facilitating conical intersections. This could possibly result in interesting dynamical effects induced by geometric phases.

V. ACKNOWLEDGEMENTS

R.S. is grateful to Matthew T. Eiles and Hans Dieter Meyer for resourceful discussions.

Appendix A: Complex absorbing potentials

Following the approach outlined in [51, 52], the CAP is implemented as a negative imaginary potential of the form

$$V_{\text{CAP}}(R) = -i\eta W(R), \quad (\text{A1})$$

$$W(R) = [R - R_c]^n \Theta(R_c - R), \quad (\text{A2})$$

where η denotes the absorption strength, R_c the onset position below which the CAP is active, n the polynomial order, and Θ the Heaviside step function. Typical choices of $n = 2-4$ yield a sufficiently smooth onset while keeping reflections minimal. Within this region, the total Hamiltonian becomes non-Hermitian,

$$H' = H - i\eta W(R), \quad (\text{A3})$$

which causes a decay of the total norm according to [51]

$$\frac{d}{dt} \|\Psi\|^2 = -2\eta \langle \Psi | W(R) | \Psi \rangle. \quad (\text{A4})$$

Hence, the decrease of $\|\Psi\|^2$ directly reflects the loss of flux into the absorbing region.

For ultralong-range Rydberg molecules, optimal CAP parameters depend on the typical kinetic energy of the nuclear wavepacket. A sufficiently weak absorber ($\eta \sim 10^{-11}$ atomic units, or $\sim 10^{-5}$ GHz) ensures that the physical dynamics in the interaction region remain unaffected while reflections are minimized. For each n -value, R_c is chosen so that the effective CAP length ($\sim 1000a_0$) far exceeds the local de Broglie wavelengths of the outgoing component to guarantee smooth absorption. In our two-channel model, the CAP is initially defined in the adiabatic representation, where it acts only within the butterfly potential channel. Upon transformation into the diabatic basis, the CAP is distributed over both diabatic components according to

$$\mathbf{V}_{\text{CAP}}^{(d)}(R) = U^\dagger(R) \begin{pmatrix} V_{\text{CAP}}(R) & 0 \\ 0 & 0 \end{pmatrix} U(R), \quad (\text{A5})$$

ensuring consistent damping of the diabatic wavepacket amplitudes.

-
- [1] C. H. Greene, A. S. Dickinson, and H. R. Sadeghpour, *Phys. Rev. Lett.* **85**, 2458 (2000).
- [2] E. L. Hamilton, C. H. Greene, and H. R. Sadeghpour, *J. Phys. B: At. Mol. Opt. Phys.* **35**, L199 (2002).
- [3] S. Hollerith, J. Rui, A. Rubio-Abadal, K. Srakaew, D. Wei, J. Zeiher, C. Gross, and I. Bloch, *Phys. Rev. Res.* **3**, 013252 (2021).
- [4] S. Hollerith, J. Zeiher, J. Rui, A. Rubio-Abadal, V. Walther, T. Pohl, D. M. Stamper-Kurn, I. Bloch, and C. Gross, *Science* **364**, 664 (2019).
- [5] Y. Q. Zou, M. Berngruber, V. S. V. Anasuri, N. Zuber, F. Meinert, R. Löw, and T. Pfau, *Phys. Rev. Lett.* **130**, 023002 (2023).
- [6] N. Zuber, V. S. V. Anasuri, M. Berngruber, Y. Q. Zou, F. Meinert, R. Löw, and T. Pfau, *Nature* **605**, 453 (2022).
- [7] D. J. Bosworth, F. Hummel, and P. Schmelcher, *Phys. Rev. A* **107**, 022807 (2023).
- [8] D. Booth, S. T. Rittenhouse, J. Yang, H. R. Sadeghpour, and J. P. Shaffer, *Science* **348**, 99 (2015).
- [9] W. Li, T. Pohl, J. M. Rost, S. T. Rittenhouse, H. R. Sadeghpour, J. Nipper, B. Butscher, J. B. Balewski, V. Bendkowsky, R. Löw, and T. Pfau, *Science* **334**, 1110 (2011).
- [10] M. Exner, R. Srikumar, R. Blättner, M. T. Eiles, P. Schmelcher, and H. Ott, *Phys. Rev. Lett.* **134**, 223401 (2025).
- [11] F. Engel, T. Dieterle, F. Hummel, C. Fey, P. Schmelcher, R. Löw, T. Pfau, and F. Meinert, *Phys. Rev. Lett.* **123**, 073003 (2019).
- [12] F. Hummel, P. Schmelcher, H. Ott, and H. R. Sadeghpour, *New J. Phys.* **22**, 063060 (2020).
- [13] S. K. Kanungo, Y. Lu, F. B. Dunning, S. Yoshida, J. Burgdörfer, and T. C. Killian, *Phys. Rev. A* **107**, 033322 (2023).
- [14] C. Fey, J. Yang, S. T. Rittenhouse, F. Munkes, M. Baluktsian, P. Schmelcher, H. R. Sadeghpour, and J. P. Shaffer, *Phys. Rev. Lett.* **122**, 103001 (2019).
- [15] C. Fey, F. Hummel, and P. Schmelcher, *Mol. Phys.* **118**, e1679401 (2020).
- [16] J. P. Shaffer, S. T. Rittenhouse, and H. R. Sadeghpour, *Nat. Commun.* **9**, 1965 (2018).
- [17] M. T. Eiles, *J. Phys. B: At. Mol. Opt. Phys.* **52**, 113001 (2019).
- [18] F. Hummel, K. Keiler, and P. Schmelcher, *Phys. Rev. A* **103**, 022827 (2021).
- [19] C. Fey, M. Kurz, and P. Schmelcher, *Phys. Rev. A* **94**, 012516 (2016).
- [20] R. Srikumar, S. T. Rittenhouse, and P. Schmelcher, *Phys.*

- Rev. A* **110**, 062808 (2024).
- [21] M. Born and R. Oppenheimer, *Ann. Phys. (Leipzig)* **389**, 457 (1927).
- [22] F. Hummel, P. Schmelcher, and M. T. Eiles, *Phys. Rev. Res.* **5**, 013114 (2023).
- [23] R. Srikumar, F. Hummel, and P. Schmelcher, *Phys. Rev. A* **108**, 012809 (2023).
- [24] F. Hummel, M. T. Eiles, and P. Schmelcher, *Phys. Rev. Lett.* **127**, 023003 (2021).
- [25] M. T. Eiles and F. Hummel, *Phys. Rev. A* **109**, 022811 (2024).
- [26] R. Srikumar, M. Exner, R. Blättner, P. Schmelcher, M. T. Eiles, and H. Ott, *Phys. Rev. Res.* **7**, 043103 (2025).
- [27] M. Schlagmüller, T. C. Liebisch, F. Engel, K. S. Kleinbach, F. Böttcher, U. Hermann, K. M. Westphal, A. Gaj, R. Löw, S. Hofferberth, T. Pfau, J. Pérez-Ríos, and C. H. Greene, *Phys. Rev. X* **6**, 031020 (2016).
- [28] F. Engel, S. K. Tiwari, T. Pfau, S. Wüster, and F. Meinert, *Phys. Rev. Res.* **6**, 033150 (2024).
- [29] A. Marciniak, V. Despré, T. Barillot, A. Rouzée, M. C. E. Galbraith, J. Klei, C.-H. Yang, C. T. L. Smeenk, V. Loriot, S. N. Reddy, A. G. G. M. Tielens, S. Mahapatra, A. I. Kuleff, M. J. J. Vrakking, and F. Lépine, *Nat. Commun.* **6**, 7909 (2015).
- [30] H. Köppel, *Chem. Phys.* **77**, 359 (1983).
- [31] W. Domcke, A. Sobolewski, and C. Woywod, *Chem. Phys. Lett.* **203**, 220 (1993).
- [32] M. F. Herman, *J. Chem. Phys.* **81**, 754 (1984).
- [33] M. Barbatti, *Wiley Interdiscip. Rev. Comput. Mol. Sci.* **1**, 620 (2011).
- [34] O. K. Rice, *J. Chem. Phys.* **1**, 375 (1933).
- [35] R. A. Harris, *J. Chem. Phys.* **39**, 978 (1963).
- [36] M. Born and K. Huang, *Dynamical Theory of Crystal Lattices* (Oxford University Press, 1954).
- [37] M. Baer, *Beyond Born-Oppenheimer: Electronic Non-adiabatic Coupling Terms and Conical Intersections* (John Wiley & Sons, Ltd, 2006).
- [38] W. Domcke, D. R. Yarkony, and H. Köppel, *Conical Intersections* (WORLD SCIENTIFIC, 2004).
- [39] F. Hummel, C. Fey, and P. Schmelcher, *Phys. Rev. A* **99**, 023401 (2019).
- [40] H. Köppel, W. Domcke, and L. S. Cederbaum, *Advances in Chemical Physics* (John Wiley & Sons, Ltd, 1984) pp. 59–246.
- [41] E. Fermi, *Nuovo Cim.* **11**, 157 (1934).
- [42] Omont, A., *J. Phys. France* **38**, 1343 (1977).
- [43] W. Li, I. Mourachko, M. W. Noel, and T. F. Gallagher, *Phys. Rev. A* **67**, 052502 (2003).
- [44] C. H. Greene and M. T. Eiles, *Phys. Rev. A* **108**, 042805 (2023).
- [45] M. T. Eiles and C. H. Greene, *Phys. Rev. A* **95**, 042515 (2017).
- [46] D. A. Anderson, S. A. Miller, and G. Raithel, *Phys. Rev. A* **90**, 062518 (2014).
- [47] S. E. Koonin, D. C. Meredith, and W. H. Press, *Computational Physics: Fortran Version* (1990).
- [48] J. Thomas, *Numerical Partial Differential Equations: Finite Difference Methods*, Texts in Applied Mathematics (Springer New York, 2013).
- [49] G. C. Groenenboom and H. M. Buck, *J. Chem. Phys.* **92**, 4374 (1990).
- [50] M. Feit, J. Fleck, and A. Steiger, *J. Comput. Phys.* **47**, 412 (1982).
- [51] H. D. Meyer, *Introduction to MCTDH*, Lecture Notes, Heidelberg University.
- [52] U. V. Riss and H. D. Meyer, *J. Phys. B: At. Mol. Opt. Phys* **26**, 4503 (1993).